Supplementary Information (SI) for Nanoscale Horizons.

Supporting Information

for

Ultra-fast WSe_2 homojunction photodiode with a large linear dynamic range towards in-sensor image processing

Shaofeng Wen, Shuren Zhou, Yimin Gong, Rui Zhang, Xinyu Jia, Lingkang Kong, Haodong Fan, Yi Yin, Changyong Lan*, Chun Li*, Yong Liu

State Key Laboratory of Electronic Thin Films and Integrated Devices, School of Optoelectronic Science and Engineering, University of Electronic Science and Technology of China, 611731, Chengdu, P. R. China

*Corresponding authors: cylan@uestc.edu.cn; lichun@uestc.edu.cn

Table of Contents

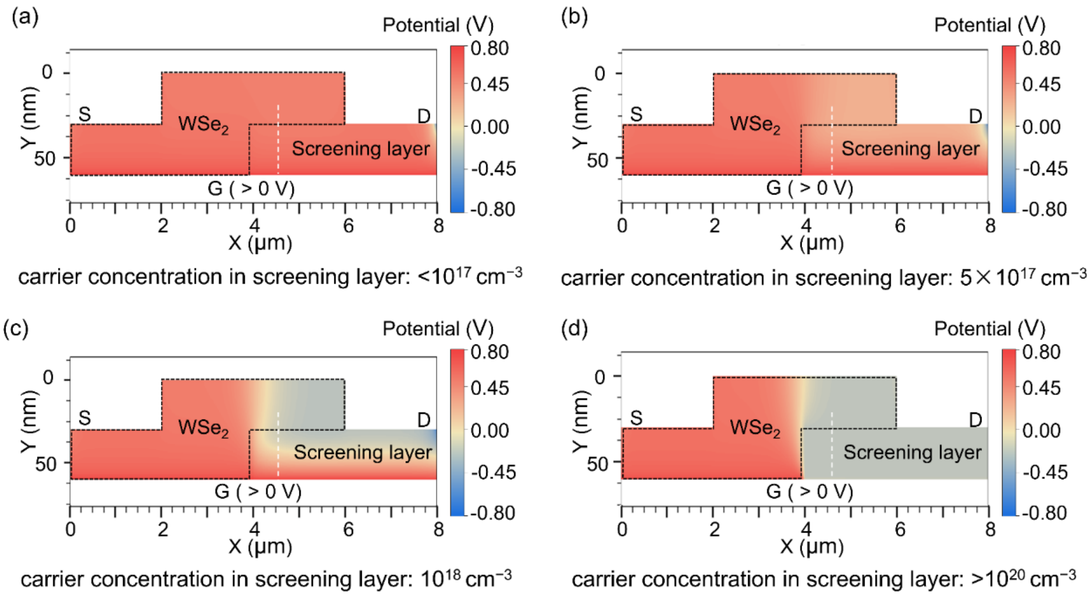

Figure S1. Silvaco TCAD simulated potential distribution in the WSe_2 in-plane homojunction for different carrier concentration in screening layer. (a) <10^{17} cm^{-3}, (b) 5×10^{17} cm^{-3}, (c) 10^{18} cm^{-3}, (d) >10^{20} cm^{-3}. V_g > 0 V, V_{ds} = 0 V. When the carrier concentration in the screening layer is larger than 10^{18} cm^{-3}, the WSe_2 in-plane homojunction can be formed.

The screening effect is affected by the carrier concentration, thickness, and permittivity of the screening layer. The Debye length expression is as follows:

$$L_D = \sqrt{\frac{\varepsilon_r k_B T}{q^2 n}}$$

where L_D is the Debye length (or screening depth), ε_r is the permittivity of the screening layer, k_B is Boltzmann's constant, T is the absolute temperature, and n is the carrier concentration per unit volume of the screening layer.

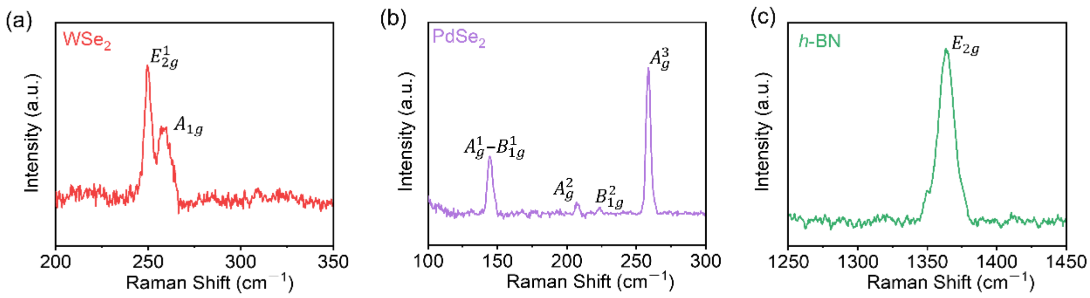

Figure S2. Raman characterization of $WSe_2/PdSe_2$/*h*-BN stacks. (a-c) Raman spectrum of the (a) WSe_2, (b) $PdSe_2$, and (c) *h*-BN. Two characteristic peaks at 249.6 and 257.1 cm^{-1} in (a), corresponding to the E_{2g}^1 and A_{1g} Raman modes of WSe_2, respectively[1,2]. Four characteristic peaks at 145.1, 207.3, 223.7, and 259.1 cm^{-1} in (b), corresponding to the $A_g^1 - B_{1g}^1$, A_g^2, B_{1g}^2 and A_g^3 Raman modes of multilayer $PdSe_2$, respectively[3–5]. And a characteristic peaks at 1364.1 cm^{-1} in (c) corresponds to the E_{2g} Raman modes of *h*-BN[1,6].

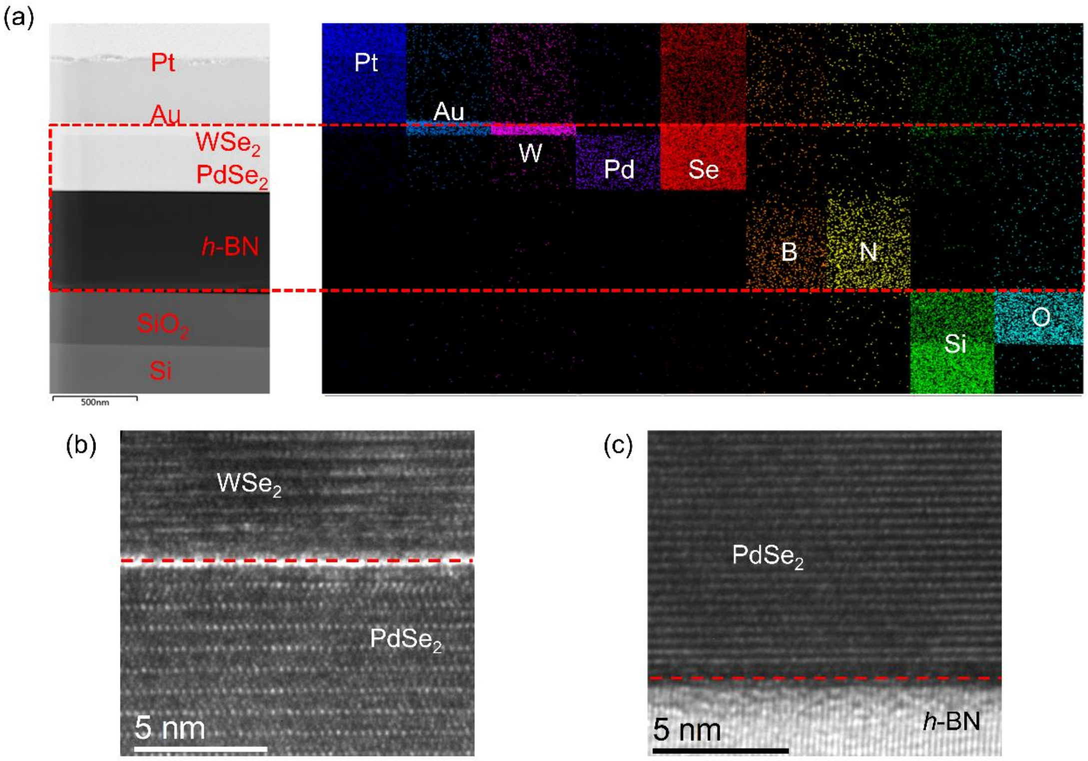

Figure S3. High-resolution transmission electron microscopy (HRTEM) characterizations and corresponding energy-dispersive spectrometry (EDS) mapping on the cross-section of the WSe_2/$PdSe_2$/*h*-BN heterostructure. (a) The scanning transmission electron microscope characterization and the EDS of the WSe_2/$PdSe_2$/*h*-BN heterostructure, which clearly shows the thickness in each layer and reveals the element mapping in each layer. (b, c) HRTEM of WSe_2/$PdSe_2$(b) and $PdSe_2$/*h*-BN (c), which confirms the clean interface between these 2D materials.

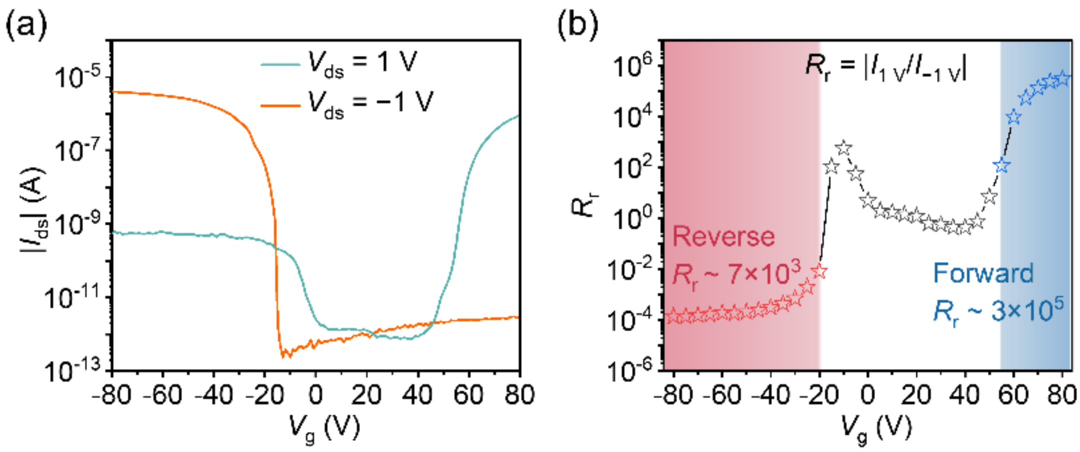

Figure S4. Electrical properties of the WSe_2 in-plane homojunction. (a) Logarithmic scale transfer curves (I_{ds}–V_g) at $V_{ds} = -1$ V (green) and 1 V (orange). (b) R_r with a function of V_g at $V_{ds} = \pm1$ V.

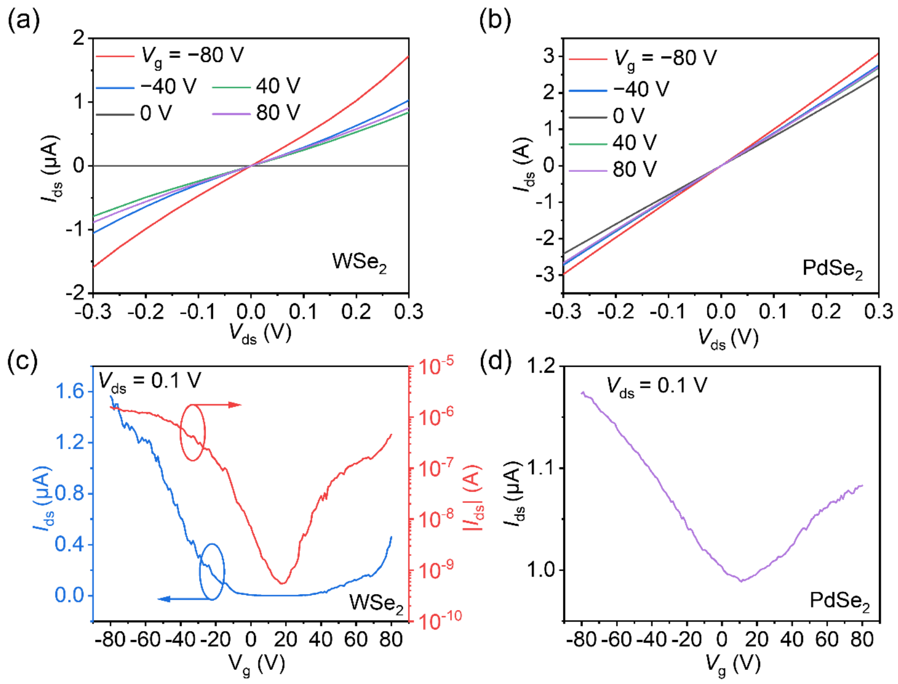

Figure S5. Output and transfer characteristics for multilayer WSe_2-FET and multilayer $PdSe_2$-FET. (a) Output characteristics of multilayer WSe_2 between the electrodes (1) and (2). (b) Output characteristics of multilayer $PdSe_2$ between the electrodes (3) and (4). (c) Transfer characteristics of multilayer WSe_2 on a linear scale (blue solid line) and a logarithmic scale (red solid line). (d) Transfer characteristics of multilayer $PdSe_2$.

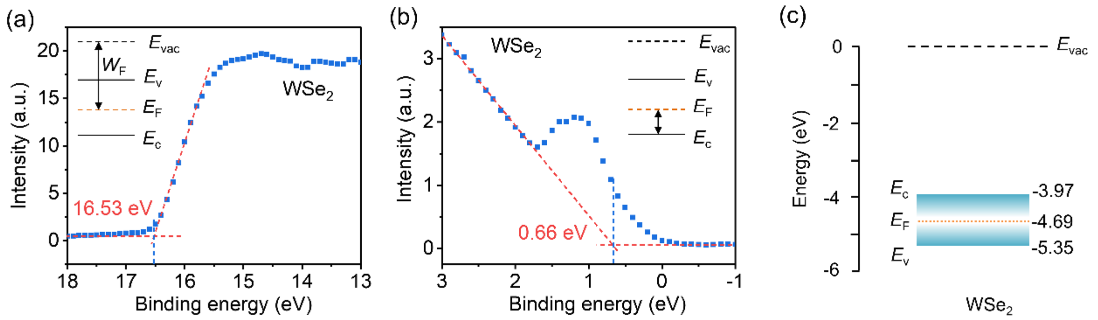

Figure S6. Ultraviolet photoelectron spectra (UPS) and band structure of WSe_2. (a, b) UPS of WSe_2 for work function and valence band edge. (c) The band structure of WSe_2. The work function (W_F) of WSe_2 was determined to be 4.69 eV, by subtracting the second electron cutoff energy from the photon energy of He I light source (21.22 eV)[7]. The valence band edge of WSe_2 was 0.66 eV, lower than their Fermi level (E_F) (binding energy equals to 0 eV). Therefore, the band structure of WSe_2 was suggested in (c) by combining the bandgap of multilayer WSe_2 (~1.38 eV)[8,9].

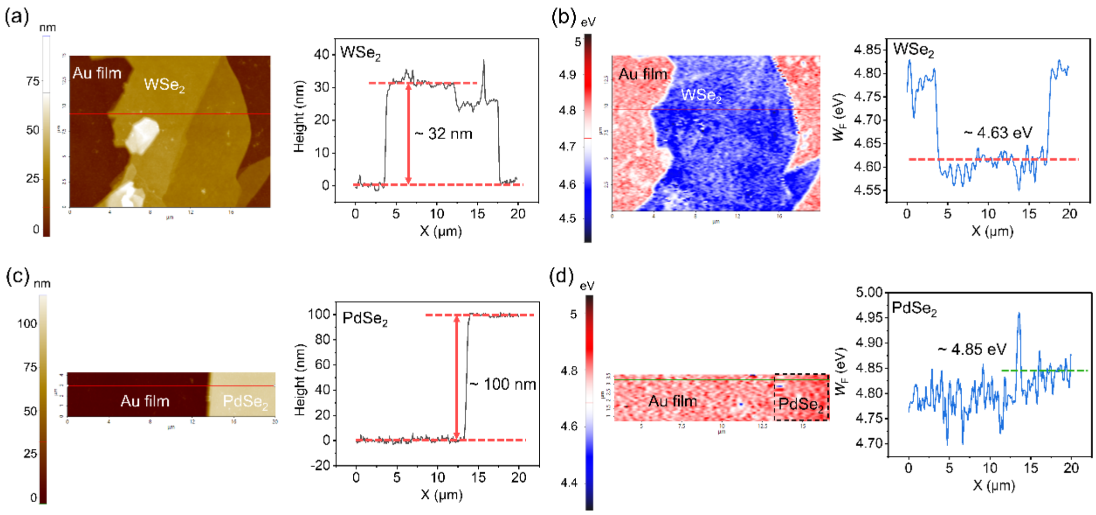

Figure S7. AFM and KPFM measurements of thick WSe_2 and thick $PdSe_2$ samples transferred on Au substrate. (a, c) The height profile of WSe_2 (a) and $PdSe_2$ (c), show the thickness of ~32 nm and ~100 nm, respectively. (b, d) The work functions of the thick WSe_2 (b) and thick $PdSe_2$ (d) are ~4.63 eV (similar to the UPS data in Figure S5) and ~4.85 eV, respectively. These results indicate a small Schottky barrier of 0.22 eV between the WSe_2 and $PdSe_2$.

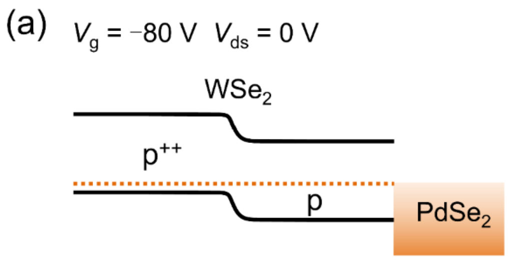

Figure S8. Band-alignment of WSe_2 in-plane homojunction at different gate voltage. (a) $V_g = -80$ V, $V_{ds} = 0$ V. (b) $V_g = 80$ V, $V_{ds} = 0$ V.

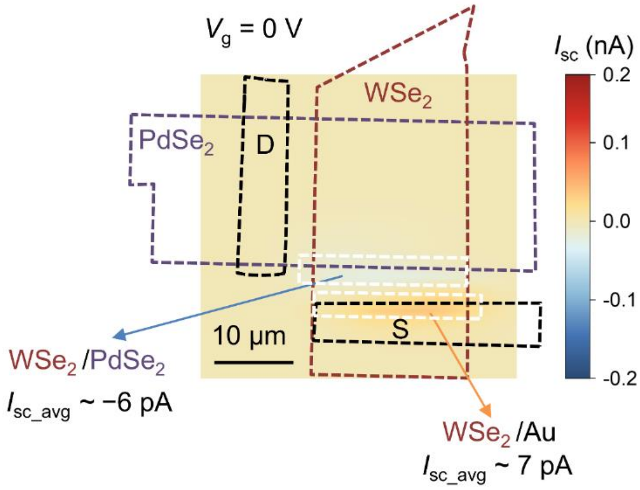

Figure S9. The scanning photocurrent mapping of the device under 520 nm at V_g = 0 V. The photocurrents of the Au/WSe_2 Schottky junction and WSe_2/$PdSe_2$ heterojunction are significantly weaker, with an average I_{sc} of −6 pA (WSe_2/$PdSe_2$ heterojunction) and 7 pA (Au/WSe_2 Schottky junction), which is approximately 20 times smaller than the average I_{sc} of the WSe_2 in-plane homojunction. (power density: 125 mW/cm^2).

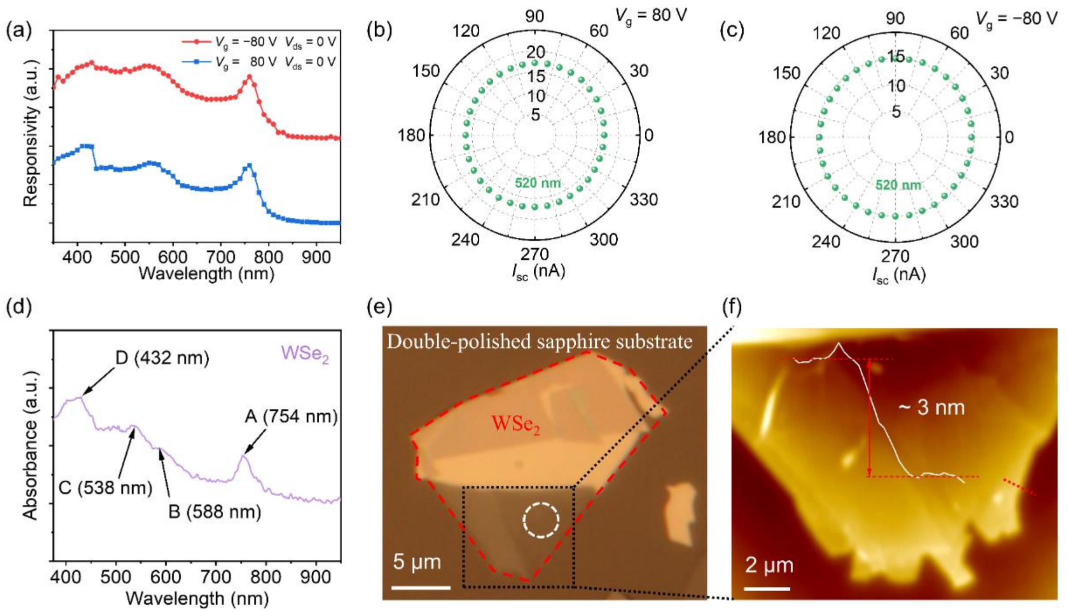

Figure S10. Spectral responsivity and polarization sensitivity of the WSe_2 in-plane homojunction device at different V_g, and absorption spectrum of WSe_2. (a) The spectral responsivity of WSe_2 in-plane homojunction device at 80 V (blue) and −80 V (red) gate voltage closely corresponds to the light absorption spectrum of WSe_2 in (d). (b, c) Polarization-free sensitivity of photocurrent in WSe_2 in-plane homojunction device (520 nm incident laser, 227 mW/cm^2). (d) Absorption spectrum of WSe_2 nanosheet. The A, B, C and D exciton peaks[10,11] are located at 754 nm, 588 nm, 538 nm and 432 nm, respectively. (e) Optical microscopy image of WSe_2 nanosheet on a double-polished sapphire substrate, where the white dashed circular area is the halogen lamp (wavelength range of 350 ~ 2200 nm, spot diameter of ~2 μm) irradiated area for absorption spectrum characterization. (f) AFM image of the WSe_2 region for absorption spectrum characterization. The inset shows the height profile along the red dashed line in (f).

The absorption spectrum can be obtained by differential reflectance spectra[12,13]. The differential reflectance spectrum is calculated as $(R_{sample} - R_{sub}) / R_{sub}$, where R_{sample} is the intensity reflected by the WSe_2 nanosheet, R_{sub} is the intensity reflected by the double-polished sapphire substrate. $(R_{sample} - R_{sub}) / R_{sub}$ is proportional to the absorption coefficient $\alpha(\lambda)$ of the WSe_2 nanosheet, when the sample thickness is much smaller than the wavelength (the thickness of WSe_2 nanosheet is less than $\lambda/100$ to avoid interference effects) and is placed on a transparent (to avoid absorption by the substrate) and uniform (to avoid noise introduced by changes in refractive index) substrate.

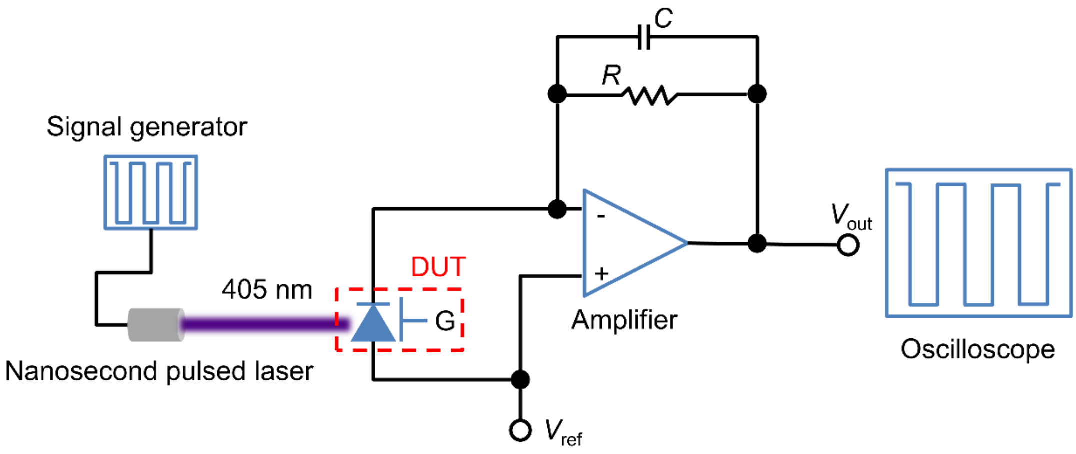

Figure S11. High-speed testing system of the device. The transient *I*–T curves of the device were obtained by a high-speed testing system consisting of a signal generator (DG852 Pro, RIGOL), a nanosecond pulsed 405 nm laser, a device under test (DUT), an amplifier (FEMTO DHPCA-100) and an oscilloscope (DHO4404, RIGOL).

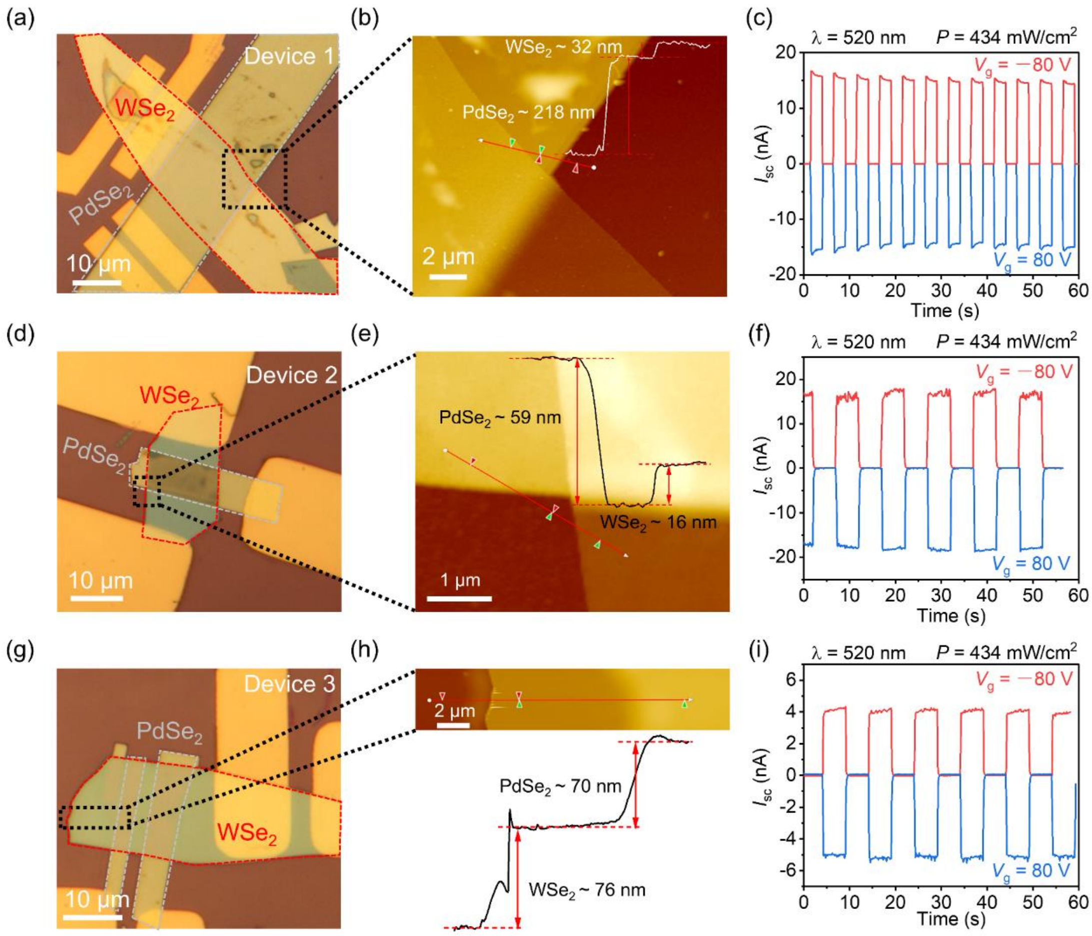

Figure S12. The reproducibility test of positive and negative photovoltaic photoresponse. (a, d, g) Optical microscopy image of two additional WSe_2 in-plane homojunction photodetectors, where the red and gray dashed regions indicate the WSe_2 and $PdSe_2$ nanosheets, respectively. (b, e, h) AFM images of the black dashed area in (a), (d) and (g). The inset shows the height profile of the WSe_2/$PdSe_2$/ stacks along the red solid line in (b), (e) and (h). (c, f, i) Positive and negative photovoltaic current–time curves under illumination at 520 nm with a power density of 434 mW/cm^2. The different I_{sc} in different devices can be attributed to differences in the area of the photosensitive region or the thickness of the material[14].

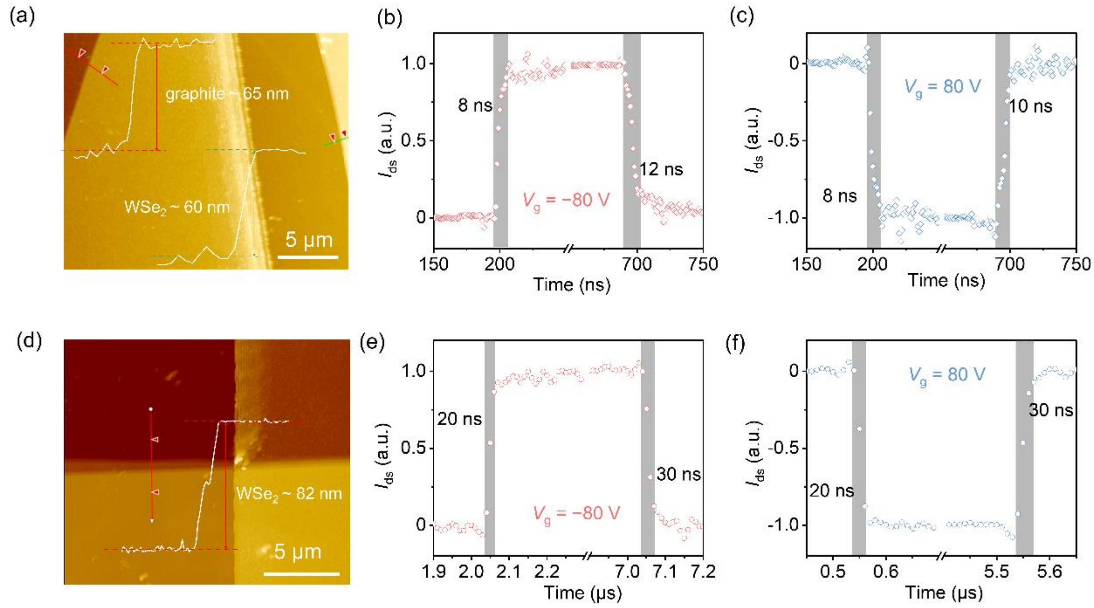

Figure S13. Demonstration of the universality by WSe2/graphite and WSe2/Au devices. (a) AFM image of the WSe2/graphite stack. The inset shows the height profile of the WSe2/thick graphite stack along the green/red solid line in (a). (b, c) Rise and fall times for positive (b) and negative (c) photovoltaic modes at nanosecond pulsed laser. (d) AFM image of the WSe2/Au stack. The inset shows the height profile of the WSe2 along the red solid line in (d). (e, f) Rise and fall times for positive (e) and negative (f) photovoltaic modes at a nanosecond pulsed laser.

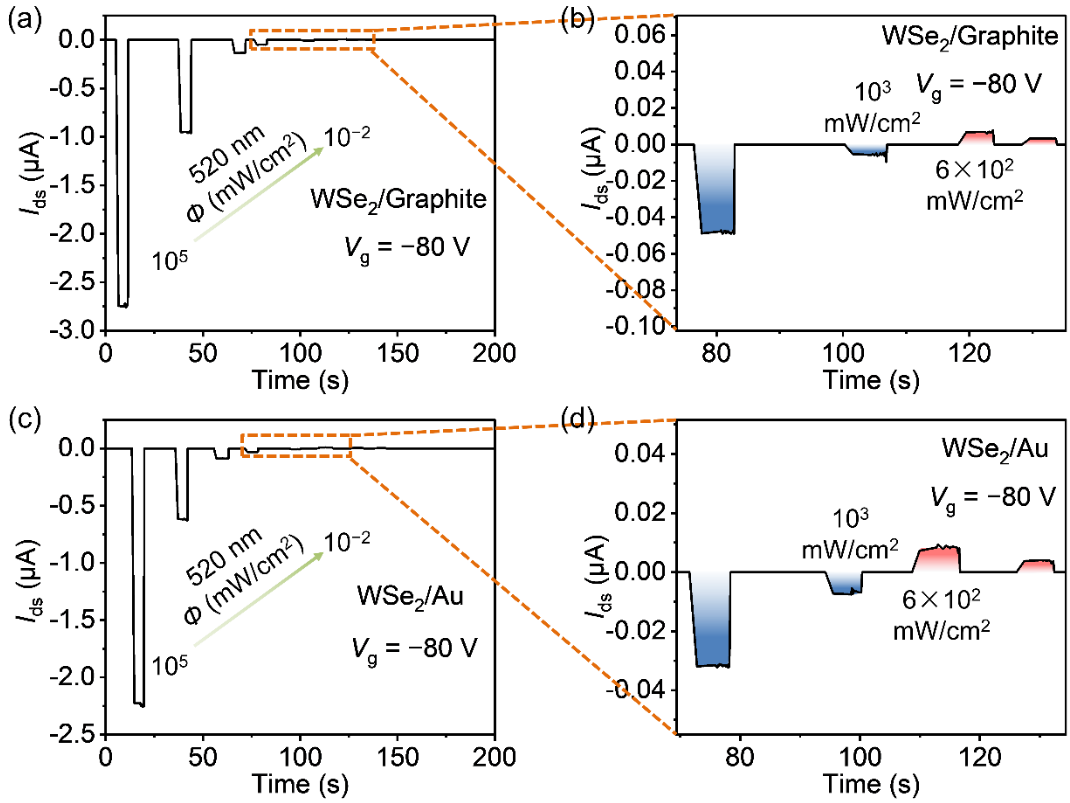

Figure S14. Power-dependent positive and negative photoresponse of WSe_2/graphite and WSe_2/Au devices. (a, b) Power-dependent positive and negative photoresponse of WSe_2/graphite stack. (b) is a magnification of the orange dashed region of (a). (c, d) Power-dependent positive and negative photoresponse of WSe_2/Au stack. (d) is a magnification of the orange dashed region of (c).

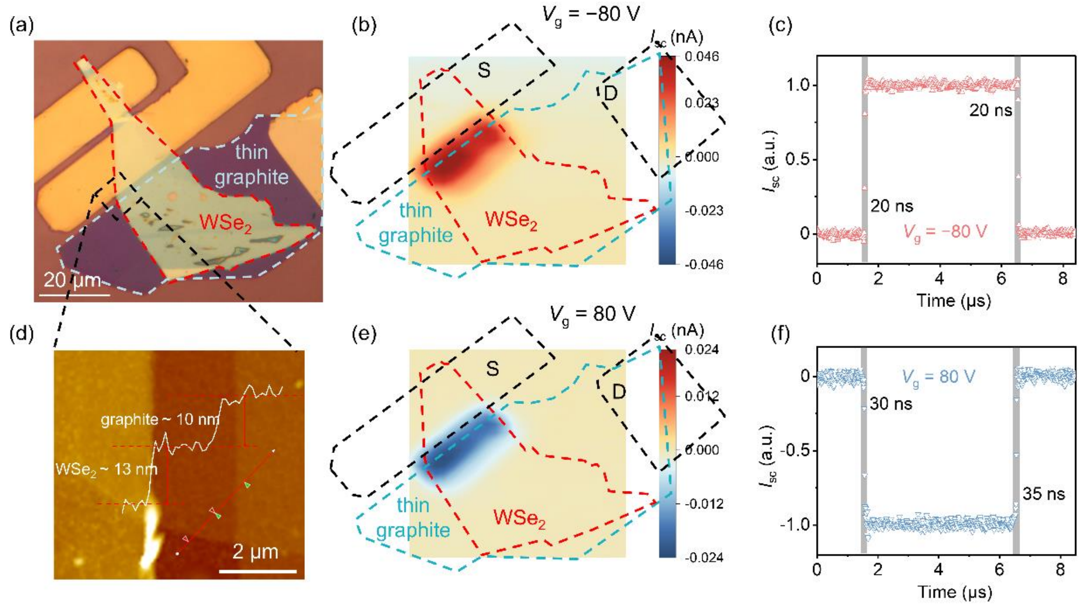

Figure S15. Demonstration of the universality by the WSe_2/thin graphite device. (a) Optical microscopy image of the WSe_2/thin graphite stack, where the thin graphite functions as the screening layer. (d) AFM image of the WSe_2/thin graphite stack. The inset shows the height profile of the WSe_2/thin graphite stack along the red solid line in (d). (b, e) The scanning I_{sc} mapping of the device under 520 nm at (c) $V_g = -80$ V and (d) 80 V, respectively. The scanning I_{sc} mapping of the device illustrates the formation of WSe_2 in-plane homojunction. (c, f) Rise and fall times for positive (b) and negative (d) photovoltaic effects at a nanosecond pulsed laser.

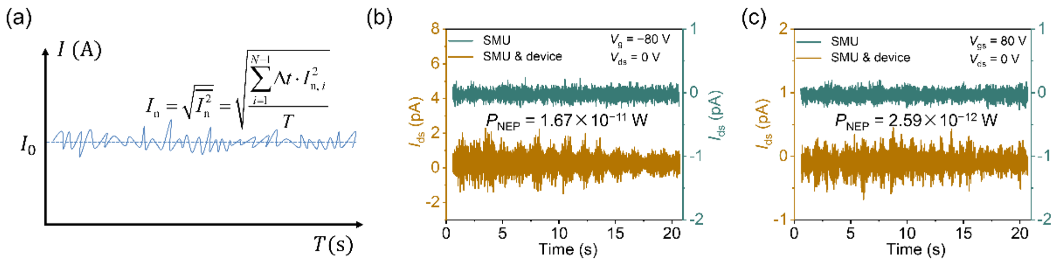

Figure S16. Noise current measurements and calculation of NEP for WSe_2 in-plane homojunction device at different V_g. (a) Schematic diagram of noise current measurement. (b) Noise current measurements of device at V_g = 80 V, V_{ds} = 0 V. (c) Noise current measurements of device at V_g = −80 V, V_{ds} = 0 V. The sampling time interval is 10 ms.

The noise current ($I_{n,\,i}$) can be calculated by these formulas:

$$I_0 = \frac{\sum_{i=1}^{N} I_i}{N} \tag{1}$$

$$I_{n,\,i} = I_i - I_0 \tag{2}$$

$$I_n = \sqrt{\overline{I_n^2}} = \sqrt{\frac{\sum_{i=1}^{N-1} \Delta t \cdot I_{n,\,i}^2}{T}} \tag{3}$$

where (t_i, I_i) is a set of current data measured in the experiment, N is the total number of data points, I_0 is the background current which can be obtained by averaging I_i (equation 1). $I_{n,\,i}$ is the noise current, Δt is the sampling time interval, and T is the total sampling time. As shown in Figure S15a, the measuring current (t_i, I_i) makes irregular undulations around background current (I_0) due to the presence of noise current ($I_{n,\,i}$). Therefore, the $I_{n,\,i}$ can be obtained by subtracting the I_0 from the I_i (equation 2). The value of noise current (I_n) cannot be obtained by averaging $I_{n,\,i}$, but it can be obtained by taking the root mean square of the $I_{n,\,i}$.

As shown in Figure S15b,c, we measured the time-current curves before (green) and after (brown) the WSe_2 homojunction device was connected to the instrument at the same voltage. By taking the root of the difference between two noise powers ($\sqrt{\overline{I^2_{\text{n, SMU\&device}}} - \overline{I^2_{\text{n, SMU}}}}$), we can obtain the noise current of the WSe_2 homojunction device ($I_{\mathrm{n,\,device}}$). Then, the equivalent noise power (P_{NEP}) of WSe_2 homojunction device can be calculated by dividing $I_{\mathrm{n,\,device}}$ by the responsivity (R) (equation 4).

$$P_{\mathrm{NEP}} = \frac{I_{\mathrm{n,\,device}}}{R} = \frac{\sqrt{\overline{I^2_{\mathrm{n,\,SMU\&device}}} - \overline{I^2_{\mathrm{n,\,SMU}}}}}{R} \tag{4}$$

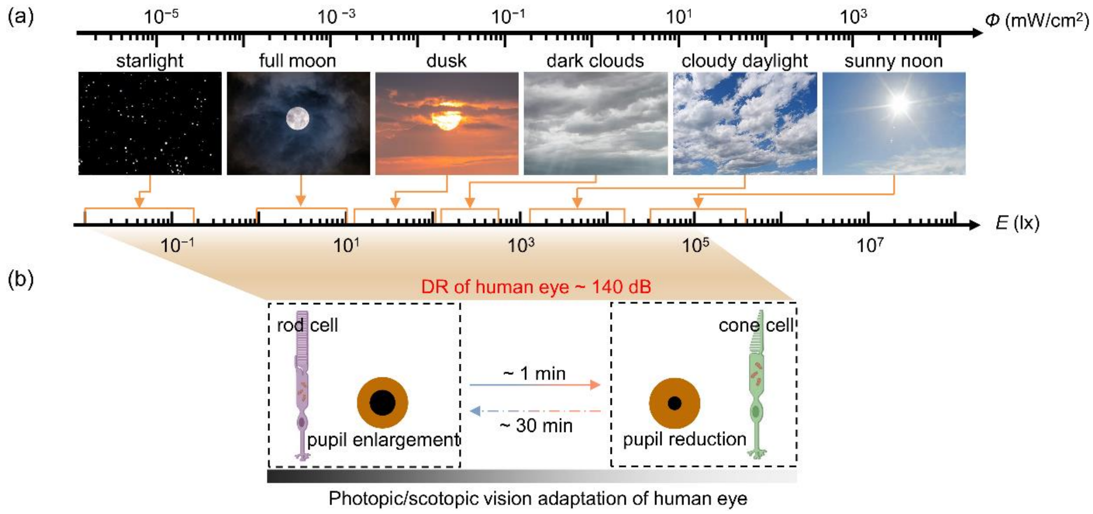

Figure S17. Illuminance levels for daily life and DR of the human eye. (a) Illuminance (E) levels for daily life (from left to right: starlight, full moon, dusk, dark clouds, cloudy daylight, and sunny noon). E is also converted with light intensity (Φ) using the peak wavelength of 555 nm according to eye-sensitive luminosity function[15]. (b) The photoreceptors in human eyes have a limited dynamic range (~40 dB)[16], but their adaptation characteristics (adjustment of retinal cells and pupil diameters) allow us to perceive and recognize various objects under different levels of illumination, from pretty dim to high brightness (~140 dB)[15,17]. However, this process of photopic/scotopic vision adaptation takes a long time (~1 min/30 min)[15].

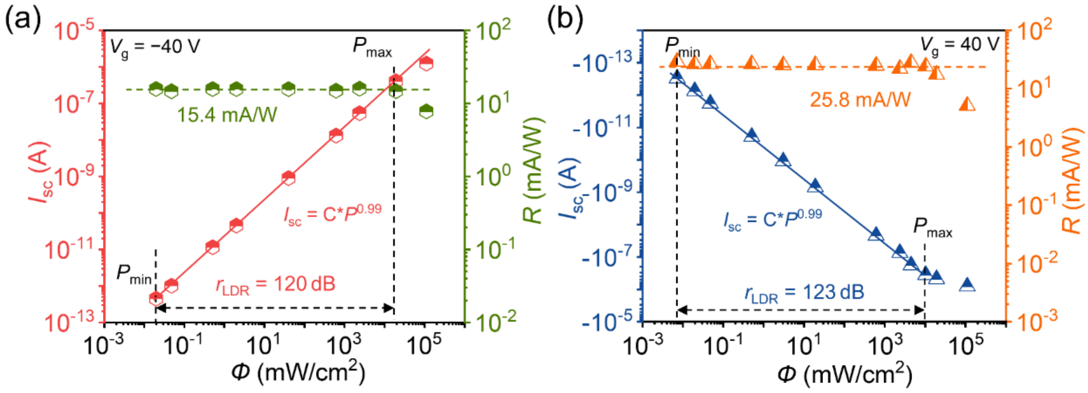

Figure S18. The large LDR of the device at multiple gate voltages. (a, b) Φ dependence of the extracted I_{sc} and responsivity at V_g of −40 V (a) and 40 V (b). The I_{sc}–Φ curves of the device exhibit nearly perfect linearity within the light power density at V_g of −40 V (a) and 40 V (b), corresponding to constant R of 15.4 mA/W (a) and 25.8 mA/W (b), respectively. The LDR values of the device are 120 dB (a) and 123 dB (b), respectively.

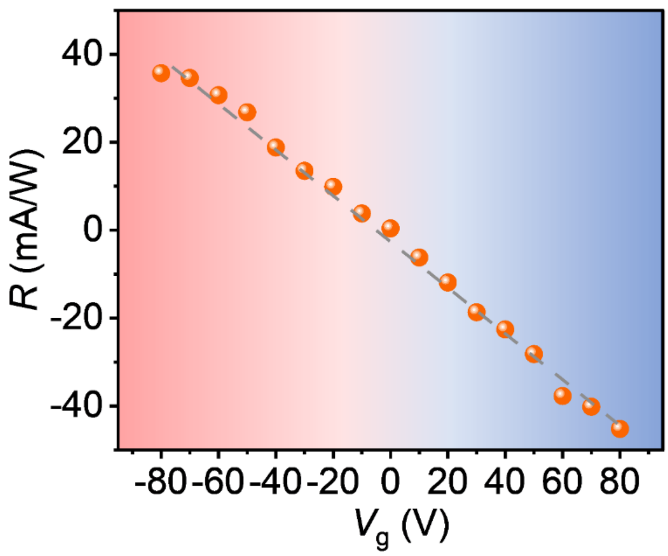

Figure S19. Gate-tunable positive and negative responsivity under illumination at 520 nm with a power density of 125 mW/cm^2. The responsivity can be tuned from negative to positive by the gate voltage, allowing for the implementation of various types of kernels.

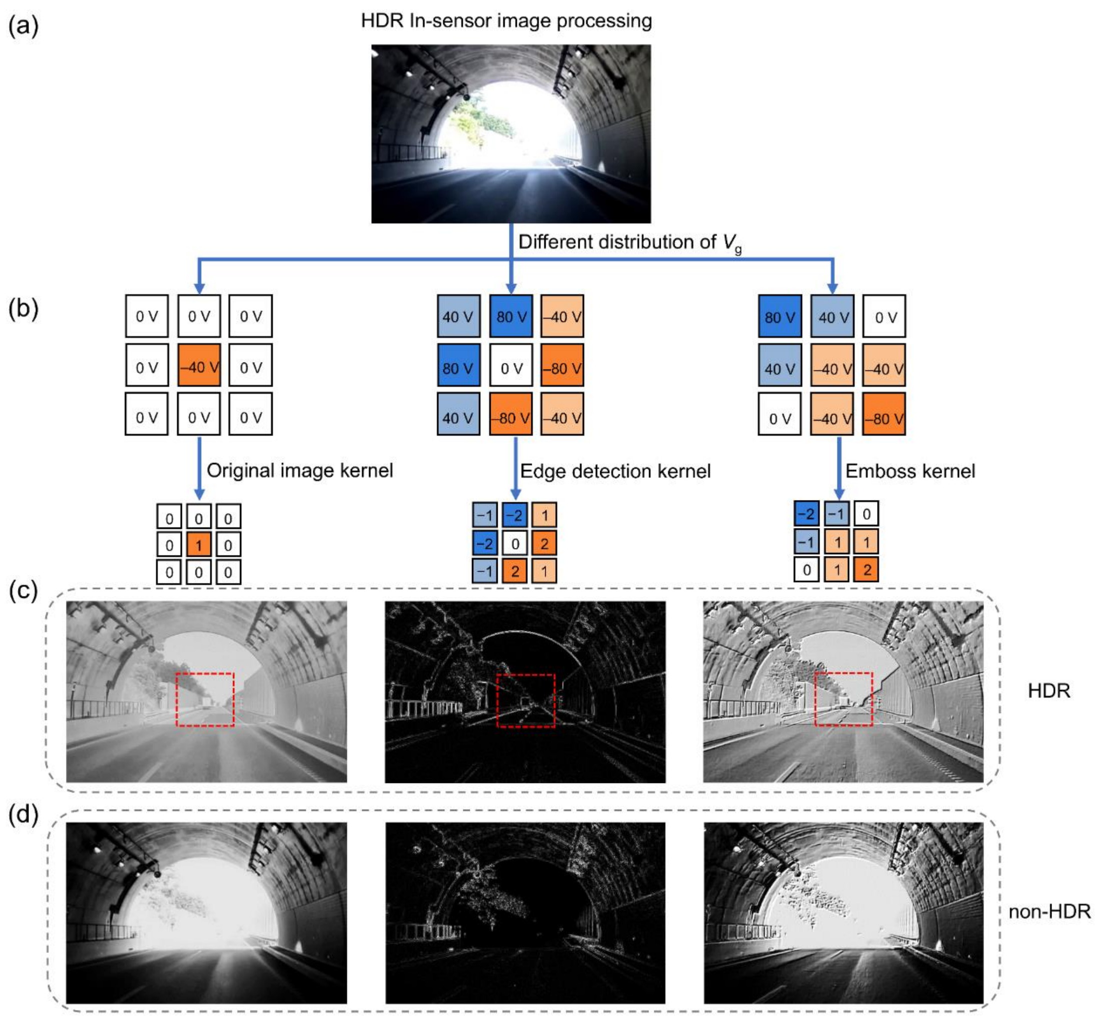

Figure S20. Simulated results of HDR in-sensor image processing. (a) Image inputs with large brightness differences. (b) HDR in-sensor visual processing demonstrating the correspondence between gate voltage and convolution kernel. From left to right corresponds to the original image, edge detection, and embossing kernel. It should be emphasized that the current gate voltage can be largely reduced by a high-*k* gate dielectric to meet the voltage requirement in digital logical circuits. (c, d) Image outputs from HDR (c) and non-HDR (d) in-sensor visual processing.

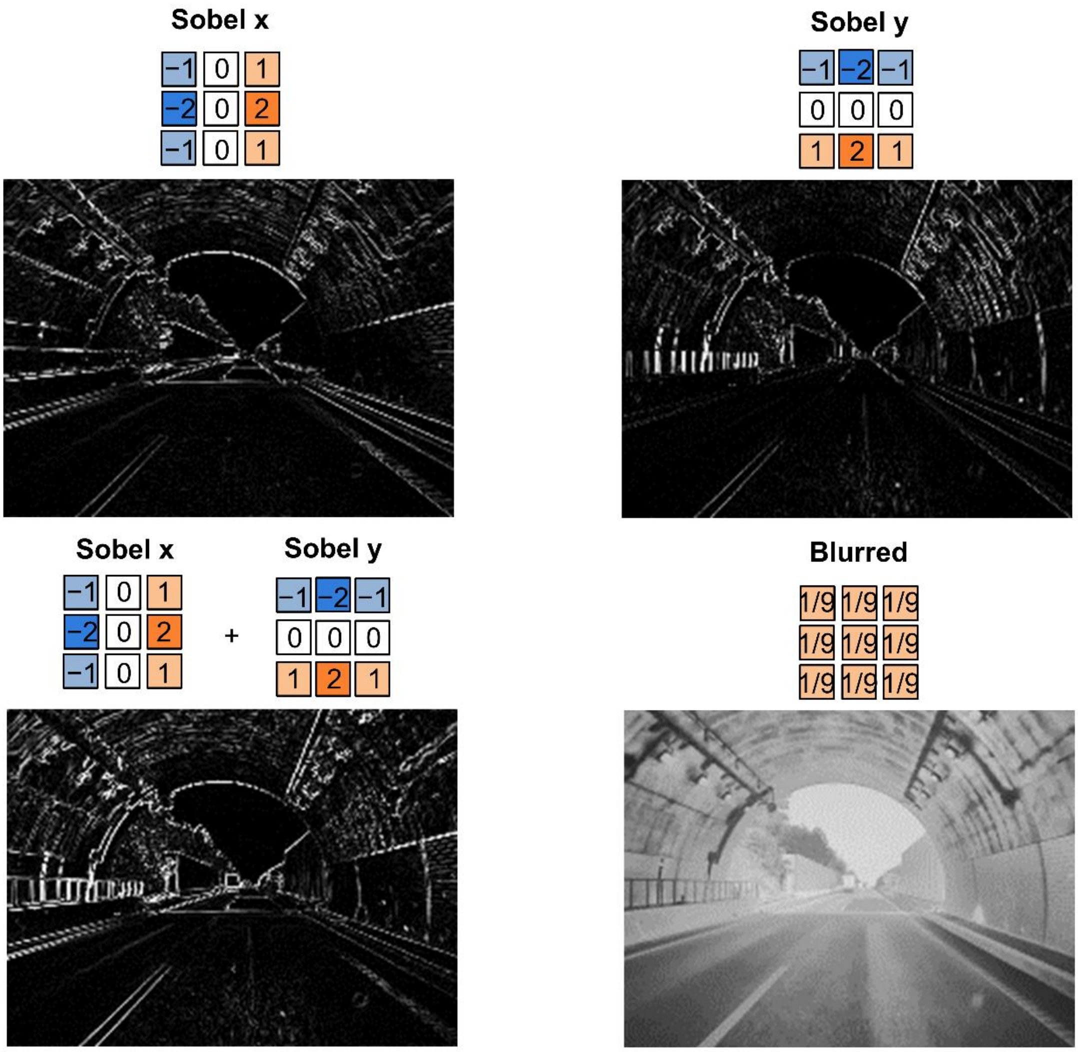

Figure S21. More modes of HDR in-sensor image processing. (a-c) Different Sobel edge enhancement operators for HDR in-sensor image processing, where (a) is the Sobel operator along the x direction, (b) is the Sobel operator along the y direction, and (c) is a combination of (a) and (b). (d) Edge blurring operators for HDR in-sensor image processing.

Table S1. The key electrical parameters of the materials for Silvaco TACD simulation (300 K).

Parameter Type	Multilayer WSe_2	Multilayer $PdSe_2$	SiO_2
dimensions (width & height)	28 μm * 30 nm	28 μm * 100 nm	36 μm * 300 nm
conductive type	semiconductor	semimetallic	insulator
electron affinity energy	−3.96 eV	−4.85 eV	−0.95 eV
bandgap	1.38 eV	0 eV	9 eV
doping type	n-type	p-type	NA
doping concentration	10^{15} cm^{-3}	10^{18} cm^{-3}	NA
electron mobility	150 $cm^2\,V^{-1}\,s^{-1}$	300 $cm^2\,V^{-1}\,s^{-1}$	NA
hole mobility	200 $cm^2\,V^{-1}\,s^{-1}$	300 $cm^2\,V^{-1}\,s^{-1}$	NA
relative permittivity (out-of-plane)	7	16	3.9

Table S2. The performance comparison (*R*, response speed and LDR) of reconfigurable photodetectors.[1,3,18–25]

Sample	Structure	λ (nm)	R (mA/W)	Response speed	LDR (dB)	Ref.
$PdSe_2/MoTe_2$	global gate	980	~32	0.4/0.4 μs	20	[20]
WSe_2/GeSe	global gate	808	NA	NA	27	[19]
$MoTe_2/WSe_2$	global gate	635	210	117/105 μs	46	[21]
$PtSe_2/WSe_2$/Au	global gate	635	316	0.83/0.95 ms	25	[22]
Si	double gate	473	~33	3/12 ns	41	[23]
$PdSe_2$	double gate	1064	1100	3/6 μs	90	[3]
WSe_2	double gate	638	NA	NA	36	[1]
WSe_2	double gate	520	50	5 μs	90	[18]
WSe_2	global gate	532	430	66.2/68.5 μs	subli near	[24]
$MoTe_2$/*h*-BN/Gr semi-floating gate	global gate	532	100	3.1/2.3 ms	73	[25]
WSe_2 −80 V	semi-screened gate	520	29.8	8/10 ns	122	This work
WSe_2 80 V	semi-screened gate	520	47.9	8/9 ns	144	This work

References

[1] Y. Wang, H. Sun, Z. Sheng, J. Dong, W. Hu, D. Tang, Z. Zhang, *Nano Res.* **2023**, *16*, 12713.

[2] E. del Corro, H. Terrones, A. Elias, C. Fantini, S. Feng, M. A. Nguyen, T. E. Mallouk, M. Terrones, M. A. Pimenta, *ACS Nano* **2014**, *8*, 9629.

[3] J. Jiang, W. Xu, F. Guo, S. Yang, W. Ge, B. Shen, N. Tang, *Nano Lett.* **2023**, *23*, 9522.

[4] L.-S. Lu, G.-H. Chen, H.-Y. Cheng, C.-P. Chuu, K.-C. Lu, C.-H. Chen, M.-Y. Lu, T.-H. Chuang, D.-H. Wei, W.-C. Chueh, W.-B. Jian, M.-Y. Li, Y.-M. Chang, L.-J. Li, W.-H. Chang, *ACS Nano* **2020**, *14*, 4963.

[5] A. D. Oyedele, S. Yang, L. Liang, A. A. Puretzky, K. Wang, J. Zhang, P. Yu, P. R. Pudasaini, A. W. Ghosh, Z. Liu, C. M. Rouleau, B. G. Sumpter, M. F. Chisholm, W. Zhou, P. D. Rack, D. B. Geohegan, K. Xiao, *J. Am. Chem. Soc.* **2017**, *139*, 14090.

[6] R. V. Gorbachev, I. Riaz, R. R. Nair, R. Jalil, L. Britnell, B. D. Belle, E. W. Hill, K. S. Novoselov, K. Watanabe, T. Taniguchi, A. K. Geim, P. Blake, *Small* **2011**, *7*, 465.

[7] P. Luo, F. Wang, J. Qu, K. Liu, X. Hu, K. Liu, T. Zhai, *Adv. Funct. Mater.* **2021**, *31*, 2008351.

[8] C. You, W. Deng, X. Chen, W. Zhou, Z. Zheng, B. An, S. Li, B. Wang, Y. Zhang, *IEEE Trans. Electron Devices* **2021**, *68*, 1702.

[9] L. Zhang, Y. Zhang, X. Sun, K. Jia, Q. Zhang, Z. Wu, H. Yin, *J. Mater. Sci.: Mater. Electron.* **2021**, *32*, 17427.

[10] N. Dong, Y. Li, Y. Feng, S. Zhang, X. Zhang, C. Chang, J. Fan, L. Zhang, J. Wang, *Sci. Rep.* **2015**, *5*, 14646.

[11] N. Ansari, F. Ghorbani, *J. Opt. Soc. Am. B* **2018**, *35*, 1179.

[12] J.D.E. McIntyre, D.E. Aspnes, *Surf. Sci.* **1971**, *24*, 417.

[13] Y. Niu, S. Gonzalez-Abad, R. Frisenda, P. Marauhn, M. Drüppel, P. Gant, R. Schmidt, N. S. Taghavi, D. Barcons, A. J. Molina-Mendoza, S. M. De Vasconcellos, R. Bratschitsch, D. Perez De Lara, M. Rohlfing, A. Castellanos-Gomez, *Nanomaterials*, **2018**, *8*, 725.

[14] H. Li, J. Wu, Z. Yin, H. Zhang, *Acc. Chem. Res.* **2014**, *47*, 1067.

[15] M. Azimipour, D. Valente, K. V. Vienola, J. S. Werner, R. J. Zawadzki, R. S. Jonnal, *Opt. Lett.* **2020**, *45*, 4658.

[16] F. Liao, Z. Zhou, B. J. Kim, J. Chen, J. Wang, T. Wan, Y. Zhou, A. T. Hoang, C. Wang, J. Kang, J.-H. Ahn, Y. Chai, *Nat. Electron.* **2022**, *5*, 84.

[17] Sony Group Portal. https://www.sony.com/en/SonyInfo/vision-s/safety.html.

[18] Y. Zhou, J. Fu, Z. Chen, F. Zhuge, Y. Wang, J. Yan, S. Ma, L. Xu, H. Yuan, M. Chan, X. Miao, Y. He, Y. Chai, *Nat. Electron.* **2023**, *6*, 870.

[19] J. Yang, Y. Cai, F. Wang, S. Li, X. Zhan, K. Xu, J. He, Z. Wang, *Nano Lett.* **2024**, *24*, 5862.

[20] L. Pi, P. Wang, S.-J. Liang, P. Luo, H. Wang, D. Li, Z. Li, P. Chen, X. Zhou, F. Miao, T. Zhai, *Nat. Electron.* **2022**, *5*, 248.

[21] H. Wang, Y. Li, P. Gao, J. Wang, X. Meng, Y. Hu, J. Yang, Z. Huang, W. Gao, Z. Zheng, Z. Wei, J. Li, N. Huo, *Adv. Mater.* **2024**, *36*, 2309371.
[22] J. Huang, K. Shu, N. Bu, Y. Yan, T. Zheng, M. Yang, Z. Zheng, N. Huo, J. Li, W. Gao, *Sci. China Mater.* **2023**, *66*, 4711.
[23] H. Jang, H. Hinton, W.-B. Jung, M.-H. Lee, C. Kim, M. Park, S.-K. Lee, S. Park, D. Ham, *Nat. Electron.* **2022**, *5*, 519.
[24] Y. Zhang, L. Wang, Y. Lei, B. Wang, Y. Lu, Y. Yao, N. Zhang, D. Lin, Z. Jiang, H. Guo, J. Zhang, H. Hu, *ACS Nano* **2022**, *16*, 20937.
[25] F. Liu, X. Lin, Y. Yan, X. Gan, Y. Cheng, X. Luo, *Nano Lett.* **2023**, *23*, 11645.

#Code S1. Silvaco TCAD simulation of potential and band energy Distributions

```
go atlas
#1. Mesh creation
x.mesh loc=0        spacing=0.1
x.mesh loc=8        spacing=0.1
y.mesh loc=0.00     spacing=0.001
y.mesh loc=0.1      spacing=0.001
y.mesh loc=0.11     spacing=0.005
y.mesh loc=0.36     spacing=0.005

#2. Material area
region number=1 user.material=WSe2    x.min=0  x.max=4  y.min=0.03
y.max=0.06
region number=2 user.material=WSe2    x.min=2  x.max=6  y.min=0
y.max=0.03
region number=3 user.material=PdSe2   x.min=4  x.max=8  y.min=0.03
y.max=0.13
region number=4 material=SiO2         x.min=0  x.max=8  y.min=0.06
y.max=0.36
region number=5 material=air

#3. Electrodes
electrode number=1 name=source x.min=0  x.max=0  y.min=0.03
y.max=0.03
electrode number=2 name=drain  x.min=8  x.max=8  y.min=0.03
y.max=0.03
electrode number=3 name=gate   x.min=0  x.max=8  y.min=0.36
y.max=0.36

#4. Doping
doping uniform conc=1e15   n.type  region=1
doping uniform conc=1e15   n.type  region=2
doping uniform conc=1e18   p.type  region=3

#5. Electrical parameters and physical modeling
material material=WSe2 user.group=semiconductor user.default=silicon eg300=1.38 \
affinity=3.97 nc300=1e19 nv300=1e19 permittivity=7 mun=150 mup=200 taun0=5e-9
taup0=5e-9 augn=1e-30 augp=1e-30
material material=PdSe2 user.group=semiconductor user.default=silicon eg300=0 \
affinity=4.85 nc300=1e19 nv300=1e19 permittivity=16 mun=300 mup=300 taun0=5e-
9 taup0=5e-9 augn=1e-30 augp=1e-30

models srh auger conmob optr fldmob print
output con.band val.band band.param
```

```
#6. Voltage setting
method newton itlimit=40 maxtraps=20
solve init
##0Vds_80Vgs
log outf=0Vds_80Vgs.log
solve vsource=0
solve vdrain=0
solve vgate=80
save outf=0Vds_80Vgs.str

##0Vds_-80Vgs
log outf=0Vds_-80Vgs.log
solve vsource=0
solve vdrain=0
solve vgate=-80
save outf=0Vds_-80Vgs.str
log off
quit
```

#Code S2. Silvaco TCAD simulation of I_{ds}–V_{ds} curves at different V_g

```
go atlas
#1. Mesh creation
x.mesh loc=0        spacing=0.1
x.mesh loc=10       spacing=0.5
x.mesh loc=26       spacing=0.1
x.mesh loc=29       spacing=0.5
x.mesh loc=36       spacing=0.5
y.mesh loc=0.00     spacing=0.001
y.mesh loc=0.03     spacing=0.001
y.mesh loc=0.13     spacing=0.002
y.mesh loc=0.33     spacing=0.002

#2. Material area
region number=1 user.material=WSe2    x.min=0   x.max=28   y.min=0   y.max=0.03
region number=2 user.material=PdSe2   x.min=8   x.max=36   y.min=0.03   y.max=0.13
region number=3 material=SiO2         x.min=0   x.max=8    y.min=0.03   y.max=0.13
region number=4 material=SiO2         x.min=0   x.max=36   y.min=0.13   y.max=0.33
region number=5 material=air

#3. Electrodes
electrode number=1 name=source x.min=0    x.max=5    y.min=0    y.max=0
electrode number=2 name=drain  x.min=31   x.max=36   y.min=0.03   y.max=0.03
electrode number=3 name=gate   x.min=0    x.max=36   y.min=0.33   y.max=0.33

#4. Doping
doping uniform conc=1e14   n.type   region=1
doping uniform conc=1e18   p.type   region=2

#5. Electrical parameters and physical modeling
material material=WSe2 user.group=semiconductor user.default=silicon eg300=1.38 \
affinity=3.97 nc300=1e19 nv300=1e19 permittivity=7 mun=150 mup=200 taun0=5e-9 taup0=5e-9 augn=1e-30 augp=1e-30
material material=PdSe2 user.group=semiconductor user.default=silicon eg300=0 \
affinity=4.85 nc300=1e19 nv300=1e19 permittivity=16 mun=300 mup=300 taun0=5e-9 taup0=5e-9 augn=1e-30 augp=1e-30

models conmob srh auger bgn fldmob CVT print
```

```
output val.band con.band qfn qfp e.field j.electron j.hole j.conduction j.total ex.field ey.field flowline e.mobility h.mobility qss e.temp h.temp j.disp

#6. Voltage setting
method newton trap
solve init
##IV_80 Vgs
log outf=IV_80Vgs.log
solve vsource=0
solve vgate=80
solve vdrain=-2 vstep=0.2 vfinal=2 name=drain
save outf=IV_80Vgs.str

##IV_-80 Vgs (doping uniform conc=1e15      p.type    region=1)
log outf=IV_-80Vgs.log
solve vsource=0
solve vgate=-80
solve vdrain=-2 vstep=0.2 vfinal=2 name=drain
save outf= IV_-80Vgs.str

log off
quit
```